

# Experimental Optimization of Current Source-Density Technique for Anuran Cerebellum

JOHN A. FREEMAN AND CHARLES NICHOLSON

*Department of Anatomy, Vanderbilt University, Nashville, Tennessee 37232; and Division of Neurobiology, Department of Physiology and Biophysics, University of Iowa, Iowa City, Iowa 52242*

ONE OF the cardinal goals in physiological studies of the central nervous system is the determination of interconnections and interactions within neuronal populations. In the previous paper (18) we presented a theoretical basis for the technique of current source-density (CSD) analysis. This technique provides a significant improvement in the ability to resolve the location and time course of neuronal activity, compared with traditional methods of analyzing extracellular potentials. From that study it was shown that the CSD can be related to the net transmembrane current  $I_m$  contributed by a population of cellular elements enclosed in an arbitrarily small volume of tissue, located at points  $(x, y, z)$  in rectangular coordinates. The CSD is given by

$$I_m(x, y, z) = - \left[ \sigma_x \frac{\partial^2 \phi}{\partial x^2} + \sigma_y \frac{\partial^2 \phi}{\partial y^2} + \sigma_z \frac{\partial^2 \phi}{\partial z^2} \right] \quad (1)$$

where measurements are made relative to the principal conductive axes of the tissue;  $\sigma_x$ ,  $\sigma_y$ ,  $\sigma_z$  are the principal conductivities; and  $\phi$  is the field potential.

In this study we consider factors involved in selecting the optimum method of CSD analysis in terms of accuracy, minimum error, and ease of application. We have compared different numerical methods for computing the spatial derivative terms in equation 1. Maximum interelectrode spacings were determined from calculations of spatial energy density spectra in the anuran cerebellum. Errors in the spacing of recording electrodes have been considered both theoretically and experimentally. The results of CSD analysis are compared to those

obtained by field potential studies in the anuran cerebellum.

## METHODS

The experimental preparation is described in the preceding paper (18).

### *Potential recording and data processing*

Potentials were either recorded with a single micropipette or with an array of six electrodes mounted in two rows of three each. The outputs of the electrodes were amplified, converted from analog to digital signals, and averaged in a PDP-12 computer (Digital Equipment Corporation). Averaged waveforms were stored on the tape or disk system of the computer. After enough data had been acquired, the CSDs were computed and displayed on a computer-driven oscilloscope or on a digital plotter.

The accuracy of electrode placement was determined in three toads by extracellular iontophoresis of 4% (weight/volume) Procion brown MX5BR (Polyscience) using 5  $\mu$ A of current, with electrode negative, for 3–5 min of dye injection, paraffin embedded, and sectioned at 20  $\mu$ m. Tissue shrinkage was estimated as less than 15% by comparison with dye-marked frozen tissue.

## THEORY AND

## EXPERIMENTAL RESULTS

### *Practical formulas for CSD analysis*

*Expression 1* can be translated into a paradigm for practical measurements. We will assume that data processing is to be carried out using a digital computer. Analog circuitry could be used also to do some or all of the computations.

Suppose that a population of nerve cells has been excited by a volley of afferent activity, which may be elicited in a repeatable manner. An array of microelectrodes

records the spatial and temporal variation in the extracellular potential distribution in the vicinity of the neuronal population. The tips of the microelectrodes are located on an imaginary, equally spaced, three-dimensional lattice (Fig. 1). The potential at each lattice point ( $x_i, y_j, z_k$ ) is recorded as a function of time  $t$  to yield a waveform  $\phi(x_i, y_j, z_k, t)$ . This waveform is sampled by an analog-to-digital converter (ADC) which breaks up the continuous waveform into a sequence of numbers representing progressive time samples of the potential at the given point.

The second spatial derivatives are approximated by a formula (D), selected from those to be described below. The derivative approximations  $D(x)$ ,  $D(y)$ ,  $D(z)$  are then weighted by the appropriate components (18) of the conductivity tensor and the CSD approximated for each sample time by

$$I_m(x_i, y_j, z_k) = -[\sigma_x D(x) + \sigma_y D(y) + \sigma_z D(z)] \quad (2)$$

This computation is then repeated for all the sample times at each point on the lattice.

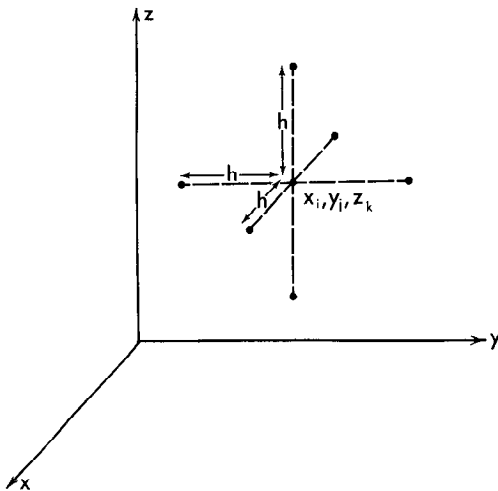


FIG. 1. Lattice for sampling potential. Measurements of potential are made at the rectangular lattice points  $x_i, y_j, z_k; x_{i+1}, y_j, z_k, \dots$  etc. Separation between lattice points (in a direction parallel to  $x, y$ , or  $z$  axis) is  $h$ . Set of points (dots) in figure constitutes the lattice for formula  $D_1$ . For the anuran cerebellum the  $x$ - $y$  plane is parallel to the cerebellar surface with  $x$  axis aligned with the direction of the parallel fibers. The  $z$  axis is parallel to the vertical axis of symmetry of the Purkinje cells.

### Aliasing

The data sampling inherent in the experiment can lead to both temporal and spatial aliasing. If a signal is sampled at a frequency  $f$ , the sampling theorem (5, 17) states that the maximum frequency component of the signal which can be reconstructed from the samples cannot exceed  $0.5f$  (and will usually be considerably lower). If frequencies greater than  $0.5f$  are present in the signal they will appear as lower frequencies after sampling, leading to signal distortion; this effect is called aliasing (5). Temporal aliasing may occur in CSD analysis through the analog-to-digital conversion procedure which has an inevitable delay between samples. This form of aliasing can be prevented by appropriate filtering of the analog signal.

Spatial aliasing arises because of the finite separation of the lattice points used for potential measurement. As with temporal sampling there is an upper limit to the spatial frequency which can be resolved. Since the lattice is intrinsic to the experimental design and potentials cannot be recorded as continuous functions of space, no filtering prior to sampling can be used. Thus the lattice spacing must be sufficiently small to resolve spatial frequencies of interest.

In order to find the maximum allowable spacing, the spatial energy density spectrum for typical cerebellar evoked potentials was measured (APPENDIX I). It was found that  $50 \mu\text{m}$  was the maximum spacing for locally evoked potentials and  $75 \mu\text{m}$  was the maximum for antidromic potentials. Thus all our data were acquired with a lattice spacing of  $50 \mu\text{m}$  or less.

### Finite-difference formulas for computing second derivative

The simplest formula for approximating the second derivative from a set of discrete data points is derived from the definition of the derivative. If  $r$  is one of the coordinates  $x, y, z$  and the other two remain constant, then parallel to the  $r$  axis successive potentials  $\phi(r-h)$ ,  $\phi(r)$ , and  $\phi(r+h)$  are encountered, where  $h$  is the lattice spacing. The first derivative at the point  $r + h/2$  is approximated by  $[\phi(r+h) - \phi(r)]/h$ ; a similar expression can be written for the deriv-

ative at  $r = h/2$ . Combining these expressions a formula for the second derivative at  $r$  is derived (Table 1):

$$D_1(r) = [\phi(r+h) - 2\phi(r) + \phi(r-h)]/h^2$$

This formula has been used in previous CSD analyses (1-4, 8, 10, 15, 19, 20) but often gives noisy results, and thus we consider other formulas which will all have the general form

$$D_l = (1/kh^2) \sum_{m=-n}^n a_m \phi(r+mh) \quad (3)$$

where  $l$  is a subscript labeling the formula and  $n$  is the largest value of  $m$  occurring in the formula.

**SIMPLE SMOOTHING FORMULA.** In order to reduce high spatial-frequency noise a symmetrical, weighted average of the potential about a given point may be used (5). This has the form

$$\bar{\phi}(r) = [b_1\phi(r+h) + b_0\phi(r) + b_1\phi(r-h)]/c \quad (4)$$

After smoothing the potentials according to this formula,  $\bar{\phi}(r)$  is substituted in the simple formula  $D_1$  to derive a new formula. The simplest smoothing formula is obtained by setting  $b_1 = 1$ ,  $b_0 = 2$ , and  $c = 4$ . This is smoothing formula  $S_1$  (Table 2) and combined with  $D_1$  it yields the second derivative formula  $D_2$ .  $D_2$  is a three-point formula like  $D_1$  since the coefficients of  $\phi(r \pm h)$  are zero.  $D_2$  can still be regarded, however, as computing the derivative relative to a lattice spacing  $h$ , although measurements are made with spacing  $2h$ .

**LANCZOS FORMULAS.** A different approach to the above was described by Lanczos (11). This author argued that derivatives of noisy data could be best performed by fitting a

polynomial to a local set of data points by the least-squares method and then differentiating the polynomial. Noise reduction would occur through the polynomial fitting, but excessive smoothing of the signal would be avoided by using only a restricted set of points for each derivative.

**Five point formula.** This formula is based on five sequential data points, symmetrically located about  $r$ . A third-degree polynomial is fitted to these points by the least-squares method and an expression derived for the second derivative of the polynomial at the point  $r$ . The choice of a cubic polynomial means that the second derivative is approximated by a first-order polynomial. This implies that the CSD cannot vary rapidly in the vicinity of a single point, thus high-frequency noise is filtered out. This procedure results in formula  $D_3$  (Table 1). It can be shown that  $D_3$  may also be regarded as a smoothing operation  $S_2$  followed by differentiation according to  $D_1$ .

**Seven- and nine-point formulas.** When five points fail to provide sufficient smoothing, more points can be incorporated and more smoothing achieved by a modification of the above approach. Using five points, a second-order polynomial is fitted by the least-squares method and the first derivative calculated. This process is then repeated on the set of derivatives. This yields a nine-point formula ( $D_5$ , Table 1) for the second derivative. By computing first derivatives at points between given lattice points (e.g.,  $r \pm h/2$ ), a second derivative over seven points can be computed ( $D_4$ , Table 1).

As in the case of  $D_3$ , expressions  $D_4$  and  $D_5$  can be regarded as a sequence of smoothing operations followed by differentiation (see Tables 1 and 2).

TABLE 1. Formulas for second derivative  $D^*$

	n	k	$a_0$	$a_{\pm 1}$	$a_{\pm 2}$	$a_{\pm 3}$	$a_{\pm 4}$	Smoothing (Table 2)
$D_1$	1	1	-2	1	0	0	0	
$D_2$	2	4	-2	0	1	0	0	$S_1 \rightarrow D_1$
$D_3$	2	7	-2	-1	2	0	0	$S_2 \rightarrow D_1$
$D_4$	3	100	-20	-5	6	9	0	$S_3 \rightarrow S_3 \rightarrow D_1$
$D_5$	4	100	-10	-4	1	4	4	$S_4 \rightarrow S_4 \rightarrow S_1 \rightarrow D_1$

$$* D_l = (1/kh^2) \sum_{m=-n}^n a_m \phi(r+mh).$$

TABLE 2. *Formulas for smoothing (weighted averaging) of potential\**

	c	b <sub>0</sub>	b <sub>1</sub>
S <sub>1</sub>	4	2	1
S <sub>2</sub>	7	3	2
S <sub>3</sub>	10	4	3
S <sub>4</sub>	5	1	2

\*  $\phi(r) = (1/c)[b_1\phi(r + h) + b_0\phi(r) + b_1\phi(r - h)]$ .

Errors

ERROR IN FORMULAS FOR SECOND DERIVATIVE. Each of the formulas D<sub>1</sub>–D<sub>5</sub> is only an approximation to the second derivative. Table 3 (APPENDIX II) shows an upper bound for the difference between an ideal second derivative and that actually performed by a given formula (column C, Table 3). In all cases as the lattice spacing, h, tends to zero, the formulas become exact second derivatives, as they should. For nonzero h, the accuracy also decreases as h<sup>2</sup> increases.

One might believe that the more accurate formulas would be the best. This is not so, however, because a study of the filtering properties of the formulas (APPENDIX III and Fig. 10) reveals that the formula inaccuracy is due to the accentuated attenuation of higher spatial frequencies. These higher frequencies are mainly noise, while the signals of interest occur at the lower frequencies. Thus the attenuation of higher spatial frequencies can actually improve the signal-to-noise ratio. This effect is shown in the results illustrated in Fig. 2.

Figure 2*A* shows a set of field potentials, recorded in the frog cerebellum at 20-μm intervals, generated by local stimulation of a narrow beam of parallel fibers. The field potentials resemble those described elsewhere (13). Figure 2*B–F* shows, respectively, the second spatial derivatives computed

with formulas D<sub>1</sub>–D<sub>5</sub>, for the z direction only. It is apparent that the waveforms produced by the D<sub>2</sub>–D<sub>5</sub> formulas are quite similar at all depths from 40 to 260 μm, whereas the corresponding results for D<sub>1</sub> show increased variability due to more differentiated high-frequency noise (see Fig. 10).

Neither the D<sub>4</sub> nor D<sub>5</sub> formulas seem to provide a significant increase in signal-to-noise enhancement for this particular set of field potentials in comparison to the D<sub>2</sub> and D<sub>3</sub> formulas. Note that the end points of formulas D<sub>3</sub> and D<sub>5</sub> are excessively noisy due to the special formulas used in these cases (11). End points are not readily computed for the other formulas.

NOISE. Noise is defined here as that component of any variable which is unrelated to its designated physiological significance, thus noise can be defined for each of the variables entering into *expression 2* and the various formulas for the second derivative. An elementary analysis of noise sensitivity of the CSD formulas is given in APPENDIX IV. Note that here we are considering how a given formula is affected by noise without regard to the question, already considered, of how well the formula approximates the second derivative. In APPENDIX IV it is shown that for a given choice of derivative formula, the error is the sum of the errors due to the potential, position, and conductivity, and that each of these errors is proportional to (error in variable) · K/h<sup>2</sup>, where K depends on the formula used (APPENDIX IV) (D<sub>1</sub> : K = 4.0, D<sub>2</sub> : K = 1.0, D<sub>3</sub> : K = 1.1, D<sub>4</sub> : K = 0.6, and D<sub>5</sub> : K = 0.4) and h is the lattice spacing. Thus error in the CSD should be linearly related to the error in the constituent variable and inversely related to the square of the lattice spacing. Increasing h will decrease error, but it will also decrease formula accuracy (see Table 3) and eventually lead to aliasing. Note that K decreases with increasing formula number and is relatively large for D<sub>1</sub>. This again indicates that formulas D<sub>2</sub>–D<sub>5</sub> are preferable. The errors in each of the variables are accessible to experimental investigation.

Noise in potential. Noise potentials which are outside the range of frequencies of physiological interest can be filtered out prior to sampling. Thus, high-frequency

TABLE 3. *Coefficients for expansion of derivative formulas\**

	A	B	C
D <sub>1</sub>	0	1	0.08Lh <sup>2</sup>
D <sub>2</sub>	0	1	0.33Lh <sup>2</sup>
D <sub>3</sub>	0	1	0.37Lh <sup>2</sup>
D <sub>4</sub>	0	1	0.68Lh <sup>2</sup>
D <sub>5</sub>	0	1	1.13Lh <sup>2</sup>

\*  $D = A\phi(r) + B\partial^2\phi(r)/\partial r^2 + R$ ;  $R \leq C$ .

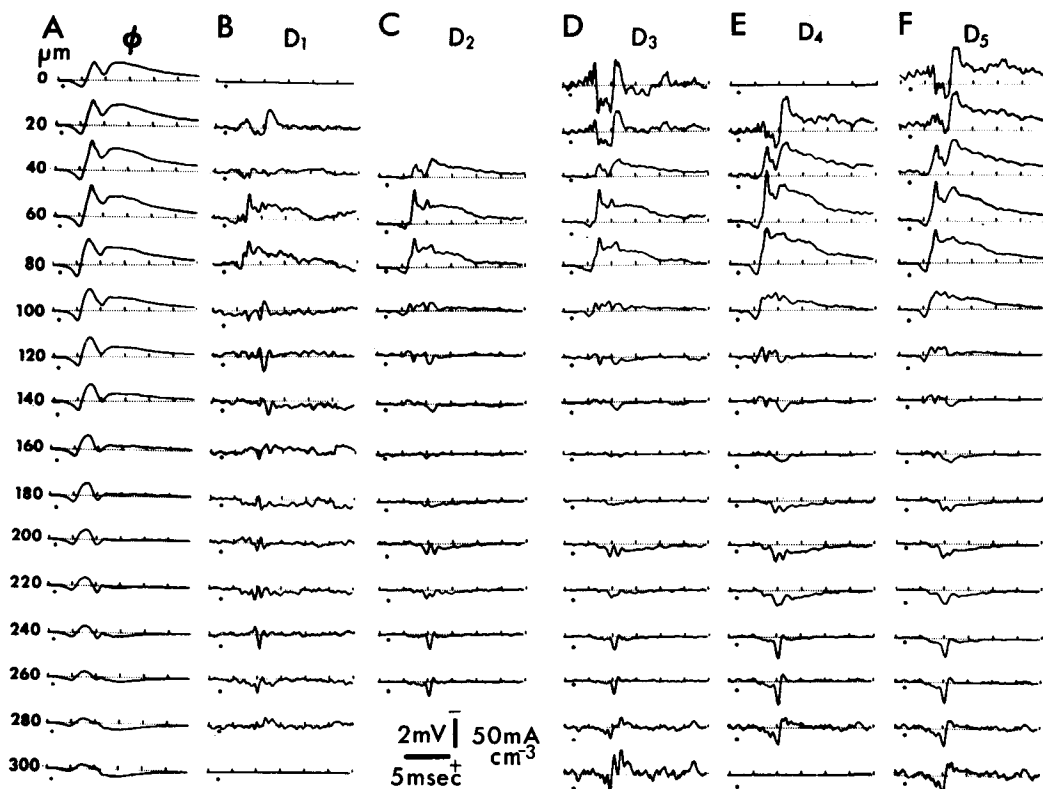


FIG. 2. Comparison of laminar field potentials and second derivatives in  $z$  direction computed by different methods. *A*: laminar field potentials produced by local stimulation of folial surface. The superficial waveform (0–100  $\mu\text{m}$ ) is a presynaptic component (parallel fiber volley) consisting of a small superficial positivity followed by a larger negativity. This is followed after a delay of approximately 2 ms by a long-lasting negativity produced by postsynaptic currents in the Purkinje cell dendrites (13). This later negative component reverses at approximately 160  $\mu\text{m}$  depth, becoming progressively more positive with increasing depth. *B–F*: second spatial derivatives for  $z$  direction computed by  $D_1$ – $D_5$  formulas. All of the smoothing formulas ( $D_2$ – $D_5$ ) considerably enhance signal-to-noise ratio. Stimuli marked by dots. Note that the top and bottom waveforms for  $D_4$  and  $D_5$  are computed with special formulas (see ref 11).

noise and low-frequency potential drift can be eliminated. The remaining noise is then within the band of frequencies which also contains the signal of interest. Even when identical stimuli are used there is usually slight, random variation in successive responses of the neuronal population. This type of error is reduced by repeating the stimulus several times and averaging the responses. This is only appropriate for events which may be evoked repeatably. This increases the signal-to-random noise ratio by a factor of  $N^{1/2}$  for  $N$  repetitions of the stimulus. During averaging it is possible to measure the standard deviation of the signal and estimate error.

The relative noisiness of each method of differentiation was evaluated by computing

the standard deviation of 50 points of the base-line record (i.e., when the tissue was not being stimulated) at each depth. The results are shown in Fig. 3. It is interesting to note that the  $D_2$  and  $D_3$  formulas produce almost equal amounts of smoothing, and that the waveforms due to both techniques are almost identical (Fig. 2C and D).

*Noise due to uncertainty in position of tip of recording electrode.* In addition to intrinsic error in the potential, mentioned above, the potential actually recorded may differ from that which was expected since it may be recorded at the wrong location.

Micromanipulators can be accurate to within  $\pm 2 \mu\text{m}$ , thus the main cause of this error is probably in the bending of the electrodes as they progress through the tissue

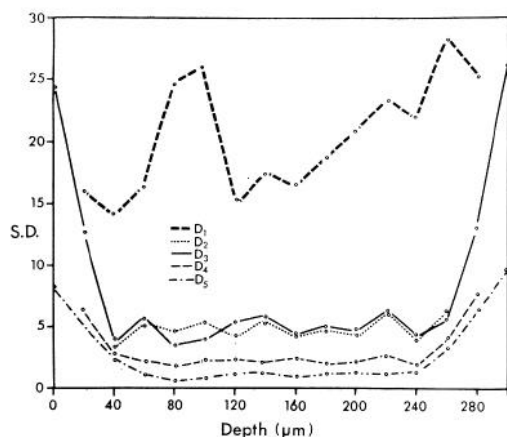


FIG. 3. Comparison of noise reduction achieved by use of different formulas for computing CSD. At each depth 50 points of the base line (no stimulus) have been averaged and the standard deviation measured. Noisiness of each method is proportional to the error (ordinate) as described in text. All the smoothing formulas significantly reduce noise.

(see ref 19, Fig. 6). For relatively superficial insertion with fine glass micropipettes this error is probably no greater than the error in the micromanipulator. This conclusion is supported by the accurate histological location (Fig. 4) of Procion brown dye marks iontophoretically placed in the tissue (see METHODS).

We investigated the noise due to erroneous electrode placement. Several sets of field potentials were recorded at 20- $\mu$ m increments in three dimensions in the anuran cerebellum, in response to stimulation of the folial surface, white matter, and the VIII nerve. The waveforms needed to compute a three-dimensional CSD, using the  $D_2$  and  $D_3$  formulas, were randomly selected from a given set of data. An initial calculation of the CSD, with no deliberate error in electrode position, was made for waveforms recorded 100  $\mu$ m apart. Subsequently waveforms corresponding to 0%, 20%, 40%, etc., spacing error were chosen and corresponding calculation errors computed. Figure 5 shows the results for field potentials produced in response to stimulation of the vestibular division of the VIII nerve. The correct CSD (using formula  $D_2$ ) is shown in Fig. 5C; Fig. 5A and B shows superimposed CSDs calculated with different spacing errors, using the  $D_2$  and  $D_3$

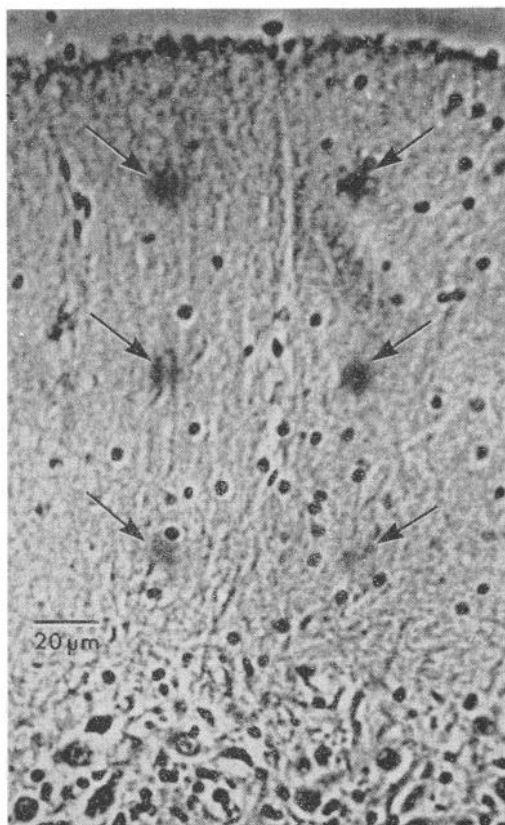


FIG. 4. Accuracy of placement of recording electrodes. Procion brown MX5BR was iontophoretically injected into the molecular layer of toad cerebellum at six locations in a frontal plane using a single electrode and a precision micromanipulator. Figure shows dye spots in fixed material (see METHODS) in one experiment where all six spots were successfully recovered and demonstrates accuracy of placement. Interelectrode spacing was 75  $\mu$ m.

formulas. The plot of calculation error versus spacing error (Fig. 5D) reveals that the CSD error rises approximately linearly with positional error, as predicted by theory (see above and APPENDIX IV). Similar results were obtained from an analysis of responses to other stimuli.

**ERRORS IN THE CONDUCTIVITY TENSOR.** When measurements are made in the principal axes, each of the three second derivatives is weighted by the appropriate conductivity value. As discussed in the previous paper (18), the situation is more complex when measurements are made in a rotated system of coordinates or when the conductivity is not constant. Assuming that these latter

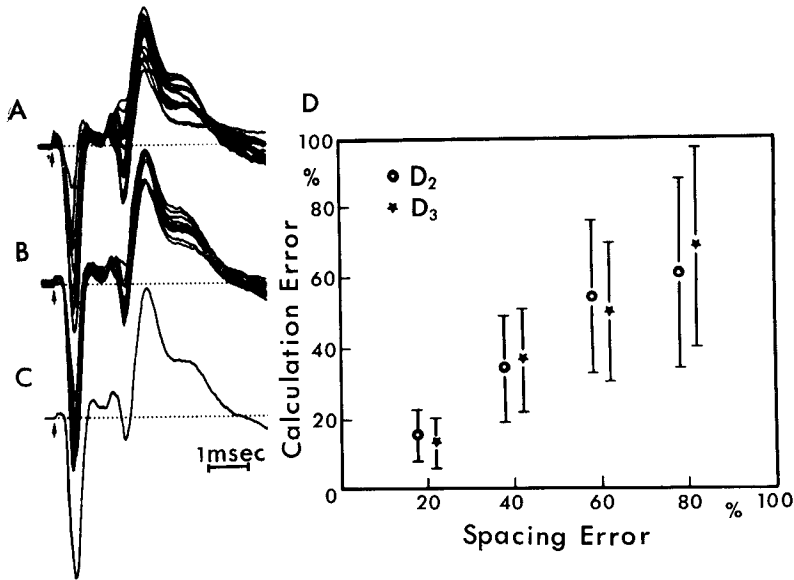


FIG. 5. Sensitivity of CSD analysis to errors in spacing of recording microelectrodes. Current source densities were computed from three-dimensional matrix of field potentials produced by vestibular nerve stimulation, at correct locations (C) and at a number of incorrect locations using formula  $D_2$  (A) and formula  $D_3$  (B). D: graph of calculation error introduced in CSD analysis by electrode spacing error. The net spacing error was defined as the square root of the sum of squares of spacing errors for all waveforms used in each calculation. The net calculation error was defined as the standard deviation between points of the "correct" CSD waveform and corresponding points of each CSD waveform with position errors. See text for further details.

sources of error are negligible, we need only consider errors in principal values of conductivity (18).

Since values of the conductivity tensor are not always available we tried to estimate the error produced by using an isotropic conductivity value instead of the correct anisotropic values.

The upper records in Fig. 6A and B show field potentials recorded at depths of 50 and 250  $\mu\text{m}$  in the toad cerebellum, in response to local stimulation. Using formula  $D_2$  and adjacent potential measurements recorded with a lattice spacing of 50  $\mu\text{m}$ , the second spatial derivatives in the  $x$ ,  $y$ , and  $z$  direction were calculated and weighted by the appropriate conductivity (18, Table 1). The three weighted second derivatives are shown in Fig. 6 to the right of the records labeled CSD. In the records corresponding to CSD', the three second derivatives were given an equal weighting corresponding to an isotropic medium of conductivity  $0.005 \text{ mho} \cdot \text{cm}^{-1}$ . The general characteristics of the CSD are unaffected by the modification of the conductivity components; however,

the relative magnitudes of different parts of the waveforms are altered, particularly in the relationship of the parallel fiber to the postsynaptic CSD (Fig. 6A).

#### *Analysis of cerebellar response to vestibular nerve stimulation*

We conclude this paper with a demonstration of the application of CSD analysis to the vestibular input of the toad cerebellum.

It has been shown that the auricular lobe of *R. catesbeiana* not only receives a direct projection from the vestibular apparatus (7, 16), but that axons of cerebellar Purkinje cells also project back to the vestibular sensory receptor (6, 7, 16). *B. marinus* has well-developed tonic labyrinthine neck and postural reflexes, both modulated by the cerebellum (unpublished results). We therefore asked whether the cerebellum and the vestibular apparatus are directly related in the toad. Figure 7A and B shows the field potentials and CSDs obtained from the auricular lobe of the toad in response to stimulation of the anterior division of the vestibular

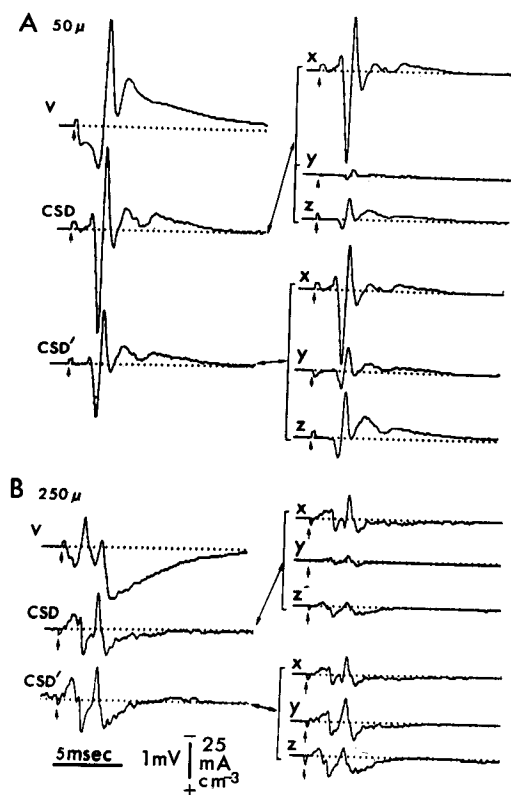


FIG. 6. Effect of anisotropy on CSD waveforms produced by parallel fiber activation. Top records of *A* and *B* show field potential ( $\phi$ ) at center point of recording matrix for 50 and 250  $\mu\text{m}$  depth. Beneath this are shown CSD records computed from sum of individual components (*X*, *Y*, and *Z*) scaled by appropriate conductivity values (CSD) and by unity (CSD'). Records to the right show components of CSD and CSD'.

nerve. The CSD analysis was based on formula  $D_2$ , with  $h = 40 \mu\text{m}$  and conductivity values for *B. marinus* described previously (18, Table 1). The field potentials reveal an early large negativity, maximum at 320  $\mu\text{m}$  depth and reversing to a small positivity at 40  $\mu\text{m}$ , closely resembling the antidromic field potentials of the frog (14). The corresponding CSD records in Fig. 7*B* show a large sink with its maximum at a depth of 320  $\mu\text{m}$ , preceded by a small source. This sink was concurrent with antidromically driven action potentials in Purkinje cell somata, recorded extracellularly. An inflection on the rising edge of the sink (arrows) is most likely the initial segment-soma dendritic (IS-SD) break of the Purkinje cell. The IS component remained with tetaniz-

ing stimuli above 100/s, at which frequency the SD component failed.

The initial negativity in the field potentials is followed approximately 3 ms later by a second prominent negativity present at all depths. The CSD waveforms show that this negativity consists of a deep sink, with maximum at a depth of 280  $\mu\text{m}$ , and another superficial sink beginning approximately 1 ms later, which increases in amplitude from a depth of 200  $\mu\text{m}$  to a maximum at 120  $\mu\text{m}$ , and decreases above that. The deeper sink is most likely produced by a mossy fiber input and subsequent granule cell depolarization. The superficial sink is probably produced by depolarization of Purkinje cells by the parallel fiber (granule cell axon) synapses.

The second set of sinks is followed in approximately 2 ms by a prominent source, maximum at a depth of 320  $\mu\text{m}$ . This source may, in part, be ascribed to repolarization of the Purkinje and granule cells; there is some evidence that there is also a contribution from active hyperpolarization of the Purkinje cells by inhibitory interneurons (deep stellate cells—which are abundant in the toad) activated by parallel fibers (unpublished results). The late source is probably also influenced by delayed afferent volleys arriving via polysynaptic pathways.

To determine conclusively whether Purkinje cell axons do project directly to the vestibular apparatus, we back-filled the vestibular nerve with Procion yellow dye by axonal iontophoresis (12). Such experiments resulted in the retrograde staining of Purkinje cells located in the ipsilateral auricular lobe.

The results illustrated in Fig. 7 demonstrate the improved ability to pinpoint neuronal inputs and outputs with CSD analysis in comparison with inspection of field potentials. This is particularly valuable in situations where a number of different incoming volleys occur simultaneously or within a short period.

## DISCUSSION

CSD analysis is a theoretically attractive method of localizing neuronal activity and determining the time course of transmembrane currents (18). To be a useful tech-



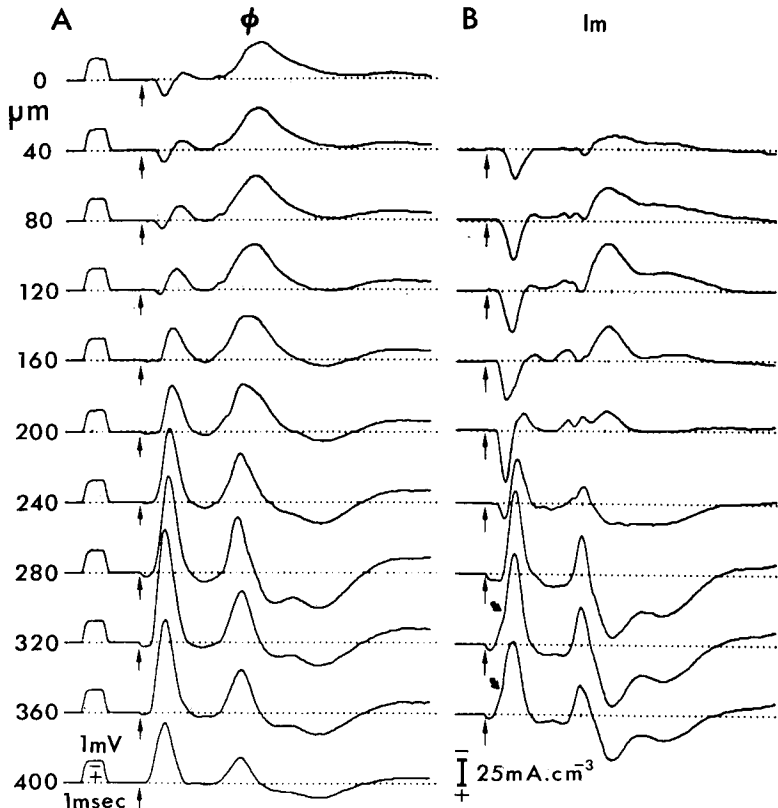


FIG. 7. Responses of toad cerebellum to vestibular nerve stimulation. *A*: field potentials consisting of early, deep negativity, ascribed to antidromic invasion of Purkinje cells and later negative-positive complex related to granule cell-Purkinje cell synaptic activation. *B*: CSD waveforms at positions corresponding to potential in *A*. Note better localization of antidromic invasion, IS-SD break (arrows at 320 and 360  $\mu\text{m}$ ), and resolution of later components of waveform into discrete events. See text for details.

nique, however, it must be capable of reliable implementation.

Since the continuous potential distribution can only be sampled at discrete points, some error is inevitable. We have shown that, for typical responses of the anuran cerebellum, the sampled points must be about 50  $\mu\text{m}$ , or less, apart for resolution of the higher spatial-frequency components of the signal. This still does not give complete resolution, since only a few samples can be taken. A lower bound on the spacing is set by the uncertainty in the recording electrode position, which probably has a fixed error of about 5  $\mu\text{m}$ ; thus spacings of 10  $\mu\text{m}$  or less incur a substantial proportional error.

Discrete sampling also means that the second derivative cannot be computed with complete accuracy. The simplest finite dif-

ference formula  $D_1$  often seems to give results which are too noisy. The noise is attenuated by formulas which provide more high spatial-frequency filtering than does  $D_1$ . Formulas  $D_4$  and  $D_5$  require seven and nine points, respectively, for their computation; often it is inconvenient to make sufficient measurements to use these formulas in three dimensions, thus we focused our attention on  $D_2$  and  $D_3$ . Our analysis of the latter formulas show that both give similar results.  $D_2$  only requires three samples in order to compute the second derivative in one dimension, however, while  $D_3$  requires five samples. Thus computation is often easier with  $D_2$ . Note that using  $D_2$  is not the same as using  $D_1$  with a spacing of  $2h$  since in the former case a set of lattice points with separation  $h$  are required in order to compute the CSD over more than one point,

while in the latter case a lattice of separation  $2h$  is used.

We have examined the formula error and noise sensitivity of  $D_1$ – $D_5$ . In general, the more accurate the formula, the more sensitive it is to noise, that is, to unwanted components of formula variables. Sensitivity also increases as the lattice spacing decreases.

Our conclusion is that  $D_2$  provides the best formula for CSD computation. In the anuran cerebellum a lattice spacing of 20–50  $\mu\text{m}$  should be used. If one is only concerned with measuring the CSD at a single point, formula  $D_2$  allows the measurements to be made at an actual spacing of  $2h$ , that is 40–100  $\mu\text{m}$ .

Ideally, simultaneous sampling of the potential at many different lattice points requires an array of microelectrodes. A simple alternative strategy is to use one electrode and to make a sequence of insertions into the tissue so that all points of the lattice are sampled. It is then necessary that the electrical activity of the tissue can be evoked repeatedly in a precisely similar manner over a sufficient period for the measurements to be accomplished. One distinction between the two approaches is that transitory "one-of-a-kind" events can only be analyzed by a multiple electrode system. The viability of either approach is essentially a practical question. We have not found evidence of significant damage to the neuronal tissue, due to the use of multiple electrode arrays. The evoked waveforms vary little on repeated penetration.

CSD analysis provides information about neuronal activity which is less ambiguous than that provided by the inspection of field potentials. As exemplified by the data on the toad vestibulocerebellar relationship, CSD analysis may enable relatively complex combinations of inputs and outputs to be quickly resolved. The price paid for this facility is a somewhat increased experimental complexity. It is quite possible that the particular choice of parameters made for the anuran cerebellum will need to be varied in other situations, but we believe that the considerations discussed in these two papers will apply.

## SUMMARY

This paper represents a systematic, semi-rigorous attempt to optimize the technique of current source-density (CSD) analysis experimentally. We compared different spatial differentiation formulas in terms of accuracy, aliasing, and smoothing, and provide experimental and theoretical rationale for their use. Sources of error have also been investigated. Expressions were derived to enable one to estimate the relative magnitude of errors due to electrical noise, uncertainty in tip position of recording electrodes, and error in the conductivity tensor. Corresponding experiments illustrating the validity of such estimates are also presented. Methods to determine the optimum inter-electrode spacing are given, based on computations of spatial energy-density spectra in the anuran cerebellum. The application of the technique of CSD analysis developed in this, and the accompanying paper, to the vestibulocerebellar input in the toad cerebellum provided significantly better temporal and spatial resolution of neuronal events than conventional field-potential analysis. Considerations germane to the optimum application of this technique to other neural structures are also discussed.

## APPENDIX I

The energy-density spectrum was calculated for field potentials generated by local stimulation of the cerebellar surface and antidromic field potentials generated by stimulation of the cerebellar white matter. Figure 8 shows a set of locally evoked field potentials used in one calculation and reveals that the waveforms undergo the greatest spatial variation at approximately 28 ms (arrows) after the stimulus. This corresponds in time to the inflection at the end of the parallel fiber volley and this instant was chosen for spectral analysis. A similar set of waveforms were constructed from antidromic field potentials.

Define the Fourier integral of the potential  $\langle\phi\rangle$  to be (5, 17)

$$\bar{\phi}(\omega) = \int_{-\infty}^{\infty} \phi(\mathbf{r}) e^{-j\omega\mathbf{r}} d\mathbf{r}$$

where  $\mathbf{r}$  is the spatial position,  $\omega$  is the spatial frequency, and  $j = \sqrt{-1}$ .

Let  $\phi(\mathbf{r})$  be regarded as zero outside an interval  $0 < r < R$ . If the above interval is subdivided into  $N$  segments, each of length  $2\mu\text{m}$ , then  $\phi(\mathbf{r})$  can be closely approximated by a set of discrete waveforms  $\phi_i$  such that

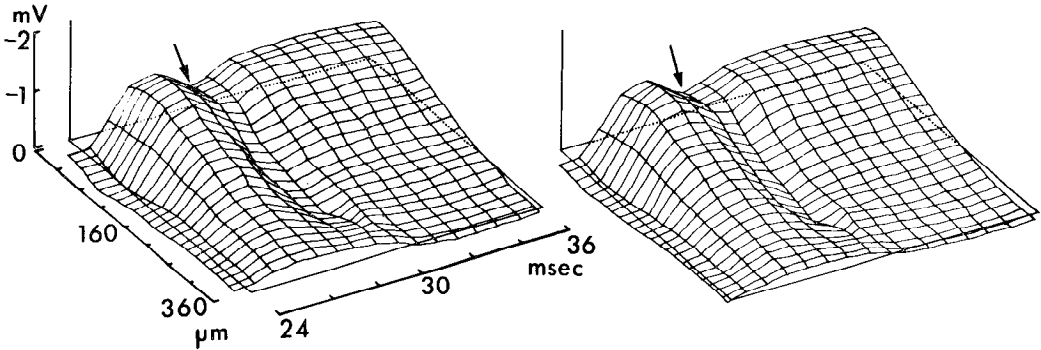


FIG. 8. Quasi-three-dimensional potential profile in anuran cerebellum produced by parallel fiber activation. Figure should be viewed as a stereopair. Arrows mark time at which maximum rate of change of potential with depth occurs; this instant was used in subsequent energy density calculations.

$$\phi_i = \hat{\phi}(r) \quad 2(i-1)u \leq r \leq 2iu \\ = 0 \quad \text{otherwise}$$

where  $\hat{\phi}(r)$  is the mean value of  $\phi(r)$  on the subinterval. Then the Fourier integral may be approximated by the sum

$$\Phi(\omega) \doteq \sum_{i=1}^N \int_{2(i-1)u}^{2iu} \phi_i e^{-j\omega r} dr \\ = \frac{2 \sin \omega u}{\omega} \sum_{i=1}^N \phi_i e^{-j\omega u(2i-1)}$$

The energy density spectrum is defined by (5, 17)

$$E(\omega) = \Phi(\omega) \cdot \Phi^*(\omega)$$

where  $\Phi^*$  is the complex conjugate of  $\Phi(\omega)$ ; hence

$$E(\omega) \doteq \left( \frac{2 \sin \omega u}{\omega} \right)^2 \left( \sum_{i=1}^N \phi_i e^{-j\omega u(2i-1)} \right) \\ \left( \sum_{k=1}^N \phi_k e^{j\omega u(2k-1)} \right) \\ = \left( \frac{2 \sin \omega u}{\omega} \right)^2 \left\{ 2 \sum_{i=1}^{N-1} \cos(2i\omega u) \right. \\ \left. \sum_{j=1}^{N-1} \phi_j \phi_{j+1} + \sum_{i=1}^N \phi_i^2 \right\} \quad (A1)$$

Using expression A1, the energy density distribution was computed<sup>1</sup> for both the parallel fiber and anti-

drismic field potentials (Fig. 9B, D). The computed values were normalized for comparison on the same scale. Most of the energy in both the parallel fiber and the antidromic field potentials is contained in the lower frequencies.

Figure 9A and C shows, respectively, the cumulative distribution of energies (ordinate) at increasing frequencies (abscissa) for the parallel fibers and for the antidromic waveforms. We have chosen a criterion level (indicated by the horizontal dashed lines) corresponding to that value of  $\omega$  (intercepted by the vertical dashed lines), above which less than 5% of the total energy is contained in each set of waveforms.

Figure 9E shows the relationship between the spatial frequency  $\omega$  and the corresponding inter-electrode distance,  $h$  ( $h = 2\pi/\omega$ ). This graph shows that the electrode spacings needed for the chosen frequencies are 100  $\mu\text{m}$  for locally evoked potential and 150  $\mu\text{m}$  for antidromic potentials. Thus by the sampling theorem (5, 17), the electrodes should be no further apart than 50 or 75  $\mu\text{m}$ , respectively. Note that our initial data were acquired with an electrode spacing of 20  $\mu\text{m}$ , thus we were unable to resolve spatial frequencies with a wavelength less than 40  $\mu\text{m}$ . The monotonically falling graph of Fig. 9 suggests, however, that there is probably very little energy at the higher frequencies.

## APPENDIX II

### Formula error

Each term  $\phi(r + mh)$  of expression 3 can be expanded as a Taylor series (9), and since expression 3 is symmetric about  $r$ , the odd terms of the expansion will cancel out leaving the expression:

$$D = \left[ (1/kh^2) \sum_{m=-n}^n a_m \right] \phi(r) \\ + \left[ (1/2k) \sum_{m=-n}^n m^2 a_m \right] \cdot \frac{\partial^2 \phi(r)}{\partial r^2} + R \quad (A2)$$

the remainder  $R$  is:

<sup>1</sup> The computation is considerably speeded up by using the relationship that:  $\cos(i\alpha) = 2 \cos(\alpha) \cos((i-1)\alpha) - \cos((i-2)\alpha)$ ,  $i = 2, 3, 4$ , etc., to calculate the cosine of integer multiples of the initial argument.

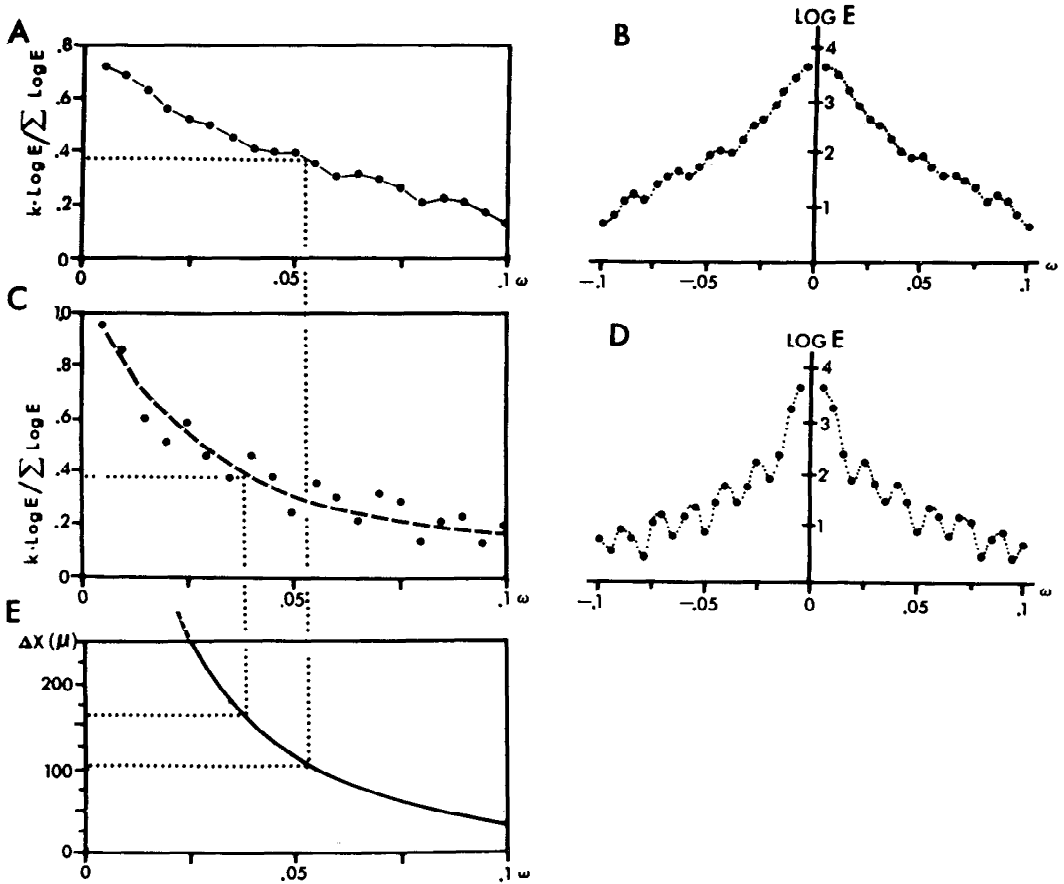


FIG. 9. Spatial energy-density spectra of extracellular field potentials. *A* and *C*: cumulative energy versus angular frequency for parallel fiber and antidromic responses explained in text. *B* and *D*: spectra for parallel fiber and antidromic responses, respectively, showing log relative energy (ordinate) versus angular spatial frequency ( $\omega$  = radians/100  $\mu\text{m}$ ). Majority of energy is contained in angular frequencies below  $\omega = 0.05$ . *E*: graph of electrode spacing ( $h$ ) (equivalent to spatial wavelength =  $2\pi/\omega$ , in micrometers) versus spatial frequency,  $\omega$ . Horizontal dashed lines show equivalent electrode spacing for frequency at which 95% of energy lies to left of graph in *A* and *C*.  $k$  is arbitrary scale factor.

$$R = (h^2/24k) \sum_{m=-n}^n m^4 a_m g_m$$

with

$$g_m = \left. \frac{\partial^4 \phi}{\partial r^4} \right|_{p_m}$$

for some  $p_m$  such that  $r - |m|h < p_m < r + |m|h$ .

Expression A2 may be written as

$$D = A\phi(r) + B \frac{\partial^2 \phi(r)}{\partial r^2} + R \quad (A3)$$

In general,  $R$  depends on  $h^2$  and the fourth derivative of the potential in a certain interval. If the fourth derivative is bounded throughout the maximum interval, say  $\leq L$ , then for each  $m$ ,  $g_m \leq L$ ,

$$\text{and then } R \leq C = (Lh^2/12k) \sum_{m=1}^n m^4 a_m. \text{ Values of}$$

$A$ ,  $B$ , and  $C$  (expression A3) are shown in Table 3.

#### APPENDIX III

##### Filtering properties of formulas for second derivative

The filtering effects of smoothing and differentiating formulas may be studied by considering their action on a band-limited function and, in particular, on the pure sinusoid (5)  $\phi(r) = \sin \omega r$  (an arbitrary signal usually may be approximated by several such sine waves, summed with appropriate magnitude and phase). Then for perfect differentiation

$$\frac{d^2 \phi}{dr^2} = -\omega^2 \sin(\omega r) \quad (A4)$$

For the general formula, expanding the sine terms, we get

$$D_s = (1/kh^2) \left\{ \sum_{m=-n}^n a_m \cos(m\omega h) \right\} \sin(\omega r) \quad (A5)$$

Comparing A4 and A5 it is seen that the term  $\omega^2$  in the exact derivative is replaced by a sum of cosine terms divided by  $kh^2$  in  $D_s$ . Thus, the original function is multiplied by a frequency-dependent function in both the exact and finite difference cases. The behavior of this function for each differentiation formula relative to the exact derivative is shown in Fig. 10. All the finite difference formulas rise in a similar way to  $\omega^2$  for low frequencies and then fall off with middle to upper frequencies. Thus, the finite difference formulas provide accurate derivatives for low frequencies and strongly attenuate high frequencies.

#### APPENDIX IV

##### Effect of noise on formulas

Let

$$I = \sigma_x D_x(x) + \sigma_y D_y(y) + \sigma_z D_z(z) \quad (A6)$$

where the  $D_i(r)$  are second spatial derivative formulas with the appropriate variable substituted for  $r$ . Suppose that there is total noise  $\Delta I$ , then the experimentally determined value of  $I$  will be  $I_e$  where

$$I_e = I \pm \Delta I \quad (A7)$$

Let the noise added to the conductivities  $\sigma_x$ ,  $\sigma_y$ , and  $\sigma_z$  be  $\pm\delta_x$ ,  $\pm\delta_y$ , and  $\pm\delta_z$ . Let the noise in

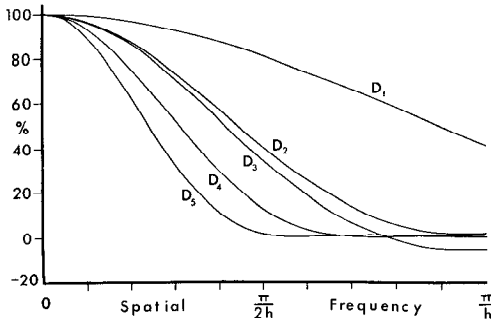


FIG. 10. Filtering properties of second-derivative formulas. Ordinate is coefficient of  $\sin \omega r$  (expression A5) divided by  $-\omega^2$  (coefficient for perfect second derivative, expression A4) and thus measures relative frequency attenuation. Abscissa is spatial frequency in radians up to the folding frequency (frequency above which aliasing occurs (5)). Figure shows that all formulas attenuate high frequencies more than low frequencies and that the more points used in computing the derivative, the greater the attenuation. Note that in formula  $D_3$  the sign of high-frequency signals is inverted as well as being attenuated; this causes a phase change.

each measurement of potential  $\phi$  be  $\pm\epsilon$ . In addition to these errors, the tip of the electrode can have a positional error

$$\Delta = (\pm\Delta_x, \pm\Delta_y, \pm\Delta_z)$$

This will introduce an error into the potential measurement, since the potential will be measured at the wrong place. This error may be approximated by the three-dimensional Taylor expansion

$$\phi(\mathbf{x} \pm \Delta) \doteq \phi(\mathbf{x}) \pm \Delta \cdot \nabla \phi(\mathbf{x}) \quad (A8)$$

From expression 3

$$\sigma_x D_x = \sigma_x (1/kh^2) \sum_{m=-n}^n a_m \phi(x + mh)$$

Let the contribution of errors from  $\sigma_x D_x$  to  $I_e$  be  $I_{ex}$ , then

$$I_{ex} \doteq (\sigma_x \pm \delta_x) (1/kh^2) \sum_{m=-n}^n a_m \{ \phi(x + mh \pm \Delta_x, y \pm \Delta_y, z \pm \Delta_z) \pm \epsilon \}$$

Similar expressions may be written for  $I_{ey}$  and  $I_{ez}$ , then using A8 and keeping only first-order error terms:

$$\begin{aligned} \Delta I = I_e - I = (1/kh^2) \sum_{m=-n}^n a_m \{ & \pm \sigma_x \Delta \cdot \nabla \phi|_{x_1} \pm \sigma_y \Delta \cdot \nabla \phi|_{x_2} \pm \sigma_z \Delta \cdot \nabla \phi|_{x_3} \\ & + \epsilon (\pm \sigma_x \pm \sigma_y \pm \sigma_z) \pm \delta_x \phi(x_1) \\ & \pm \delta_y \phi(x_2) \pm \delta_z \phi(x_3) \} \end{aligned} \quad (A9)$$

where  $x_1 = (x + mh, y, z)$ ,  $x_2 = (x, y + mh, z)$ ,  $x_3 = (x, y, z + mh)$ .

This expression may be simplified if the following assumptions are made:

$$1) \quad \Delta_x = \Delta_y = \Delta_z = \Delta$$

$$2) \quad \sigma_x = \sigma_y = \sigma_z = \sigma$$

$$3) \quad \delta_x = \delta_y = \delta_z = \delta$$

$$4) \quad \left| \frac{\partial \phi}{\partial r} \right| \leq M \text{ for } r = x, y, z$$

$$5) \quad |\phi(\mathbf{x})| \leq N$$

Assumptions 4 and 5 imply that the current flow and potential have finite values, which is physiologically correct. Then

$$|\Delta I| \leq E_1 + E_2 + E_3$$

where

$$E_1 = (9M\Delta\sigma/h^2)K$$

$$E_2 = (3\sigma\epsilon/h^2)K$$

$$E_3 = (3\delta N/h^2)K$$

and

$$K = (1/k) \sum_{m=-n}^n |a_m| \quad (A10)$$

$E_1$  gives a bound on the error due to misplacement of electrodes;  $E_2$ , error due to noise in the potential; and  $E_3$ , error due to inaccuracy in the conductivity tensor. This discussion assumes that measurements are made with reference to the principal axes. If this is not so, more complex error

analysis may be required based on the more general formula for the CSD (equation A8, ref 18).

#### ACKNOWLEDGMENTS

We are indebted to Dr. R. Llinás for his encouragement during this project and to Dr. J. Stone for his participation in the early phase of the work.

Research was supported by Public Health Service Grants E-40117 to J. A. Freeman and NS-09916 to C. Nicholson.

#### REFERENCES

1. FREEMAN, J. A. AND STONE, J. A technique for current density analysis of field potentials and its application to the frog cerebellum. In: *Neurobiology of Cerebellar Evolution and Development*, edited by R. Llinás. Chicago: Am. Med. Assoc., 1969, p. 421-430.
2. HABERLY, L. B. AND SHEPHERD, G. M. Current-density analysis of summed evoked potentials in opossum prepyriform cortex. *J. Neurophysiol.* 36: 789-803, 1973.
3. HAGINS, W. A. Electrical signs of information flow in photoreceptors. *Cold Spring Harbor Symp. Quant. Biol.* 30: 403-418, 1965.
4. HAGINS, W. A., PENN, R. D., AND YOSHIKAMI, S. Dark currents and photocurrent in retinal rods. *Biophys. J.* 10: 380-412, 1970.
5. HAMMING, R. W. *Numerical Methods for Scientists and Engineers*. New York: McGraw, 1962.
6. HILLMAN, D. E. Efferent vestibular fibers in the frog. *Progr. Brain Res.* 37: 445-448, 1972.
7. HILLMAN, D. E. Vestibulo cerebellar input in the frog: anatomy. *Progr. Brain Res.* 37: 329-339, 1972.
8. HOWLAND, B., LETTVIN, J. Y., MCCULLOCH, W. S., PITTS, W., AND WALL, P. D. Reflex inhibition by dorsal root interaction. *J. Neurophysiol.* 18: 1-17, 1955.
9. KORN, G. A. AND KORN, T. M. *Mathematical Handbook for Scientists and Engineers*. New York: McGraw, 1968.
10. KORNACKER, K. Some properties of the afferent pathway in the frog corneal reflex. *Exptl. Neurol.* 7: 224-239, 1963.
11. LANCZOS, C. *Applied Analysis*. Englewood Cliffs, N.J.: Prentice Hall, 1956.
12. LLINÁS, R. Procion yellow and cobalt as tools for the study of structure-function relationships in vertebrate control nervous system. In: *Intracellular Staining in Neurobiology*, edited by S. B. Kater and C. Nicholson. New York: Springer, 1973, p. 211-225.
13. LLINÁS, R., BLOEDEL, J. R., AND HILLMAN, D. E. Functional characterization of neuronal circuitry of frog cerebellar cortex. *J. Neurophysiol.* 32: 847-870, 1969.
14. LLINÁS, R., BLOEDEL, J. R., AND ROBERTS, W. Antidromic invasion of Purkinje cells in frog cerebellum. *J. Neurophysiol.* 32: 881-891, 1969.
15. LLINÁS, R. AND NICHOLSON, C. Electrophysiological analysis of alligator cerebellar cortex: a study of dendritic spikes. In: *Neurobiology of Cerebellar Evolution and Development*, edited by R. Llinás. Chicago: Am. Med. Assoc., 1969, p. 431-465.
16. LLINÁS, R. AND PRECHT, W. Vestibulocerebellar input: physiology. *Progr. Brain Res.* 37: 341-359, 1972.
17. MASON, S. J. AND ZIMMERMANN, M. J. *Electronic Circuits, Signals and Systems*. New York: Wiley, 1960.
18. NICHOLSON, C. AND FREEMAN, J. A. Theory of current source-density analysis and determination of conductivity tensor for anuran cerebellum. *J. Neurophysiol.* 38: 356-368, 1975.
19. PITTS, W. Investigations on synaptic transmission. In: *Cybernetics, Trans. 9th Conf.*, edited by H. von Foerster. New York: Josiah Macy, 1952, p. 159-162.
20. STONE, J. AND FREEMAN, J. A. Synaptic organization of pigeon's optic tectum: a Golgi and current source-density analysis. *Brain Res.* 27: 203-221, 1971.